Design and Stiffness Control of a Variable-Length Continuum Robot for Endoscopic Surgery

Jingyu Zhang, *Member, IEEE*, Qin Fang, Lilu Liu, Rui Jin, Pingyu Xiang, Rong Xiong, *Senior Member, IEEE*, Yue Wang, *Member, IEEE*, and Haojian Lu, *Member, IEEE*

***Abstract*— Continuum robots, owing to their inherent compliance, have become essential in endoscopic surgical procedures, such as mucosal ablation. However, the prevalent design of endoscopic manipulators, which typically features only a single active bending segment, often results in limited dexterity and accessibility. Additionally, the incorporation of variable stiffness in these robots has attracted significant interest, with the aim to improve manipulation capabilities in confined spaces. In the paper, we propose a novel variable-length continuum robot with variable stiffness for endoscopic surgery. The robot's stiffness can be altered either by modifying the catheter's length or solid-liquid transition of low-melting-point alloy (LMPA). The design and fabrication methods of the robot are meticulously detailed. Additionally, a quasi-static stiffness model along with a learning-based stiffness compensation approach for accurate stiffness estimation are proposed. Leveraging this model, a contact force controller is designed for ablation procedure. The experimental results show that our robot possesses good flexibility and accessibility, making it highly adept at manipulating in confined spaces. Its variable stiffness feature significantly enhances its ability to counteract external disturbance and prevent tip deformation (with a average position change of 1.1mm). Finally, through force control experiments and a surgical demonstration in a gastrointestinal model, we have further validated the robot's applicability in surgical contexts.**

***Note to Practitioners*—This paper proposed a variable-length continuum robot with variable stiffness for endoscopic surgery. The robot can achieve axial elongation and omnidirectional bending motion, having better dexterity and accessibility than traditional medical continuum robots with one active bending segment. The robot's stiffness can be adjusted by the length changes or solid-liquid transition of low-melting-point alloy (LMPA). Besides, an accurate stiffness model and a contact force controller are proposed for endoscopic ablation surgery. By experimental results, the robot shows high flexibility and accessibility, allowing access to confined spaces for manipulation, and good control accuracy and variable stiffness capability for endoscopic surgery.**

***Index Terms*— Soft robots, small-scale robot, variable length, variable stiffness, endoscopic surgery.**

Manuscript received 5 February 2024; revised 2 May 2024; accepted 17 June 2024. This article was recommended for publication by Associate Editor H. Wang and Editor L. Zhang upon evaluation of the reviewers' comments. This work was supported in part by Zhejiang Provincial Natural Science Foundation of China under Grant LD22E050007, in part by the National Natural Science Foundation of China under Grant 62303407 and Grant 62103363, and in part by the Key Research and Development Program of Zhejiang under Grant 2022C01022 and Grant 2023C01176. *(Jingyu Zhang and Qin Fang contributed equally to this work.) (Corresponding authors: Haojian Lu; Yue Wang.)*

Jingyu Zhang, Qin Fang, Lilu Liu, Rui Jin, Pingyu Xiang, Rong Xiong, and Yue Wang are with the State Key Laboratory of Industrial Control and Technology and the Institute of Cyber-Systems and Control, Zhejiang University, Hangzhou 310027, China (e-mail: ywang24@zju.edu.cn).

Haojian Lu is with the State Key Laboratory of Industrial Control and Technology and the Institute of Cyber-Systems and Control, Zhejiang University, Hangzhou 310027, China, and also with Stomatology Hospital, the School of Stomatology, Zhejiang Provincial Clinical Research Center for Oral Diseases, the Key Laboratory of Oral Biomedical Research of Zhejiang Province, the Cancer Center of Zhejiang University, and the Engineering Research Center of Oral Biomaterials and Devices of Zhejiang Province, Zhejiang University School of Medicine, Hangzhou 310000, China (e-mail: luhaojian@zju.edu.cn).

This article has supplementary material provided by the authors and color versions of one or more figures available at https://doi.org/10.1109/TASE.2024.3418092.

Digital Object Identifier 10.1109/TASE.2024.3418092

I. Introduction

CONTINUUM robots, drawing inspiration from the snakes [1], elephant trunks [2], and tendrils [3], [4], are becoming increasingly prevalent in the realm of endoscopic surgery [5]. Their unique ability to bend flexibly and form continuous shapes allows them to navigate through confined spaces. Recent developments have seen the creation of several continuum robots with a single active bending segment, aimed at transforming treatment methodologies in various medical fields such as cardiology [6], [7], pulmonology [8], [9], and urology [10]. Nonetheless, these robots still face challenges related to their limited dexterity and accessibility, which can hinder effective disease diagnosis and treatment within the confined confines of human anatomy.

To expand their operational range and enhance flexibility, advancements in continuum robot design have led to the development of models featuring two or more active bending segments. For instance, Hong et al. developed a two-segment continuum robot for maxillary sinus surgery [11], Wang et al. developed a flexible tendon-driven continuum manipulator for laparoscopic surgery [12], Zeng et al. developed a two-segment notched continuum Robot for sinus surgery [13], and Alfalahi et al. developed a three-segment hand-held concentric tube robot for minimally invasive surgery [14]. However, the tracking errors of these robots will gradually accumulate with an increasing number of segments, and more actuators are necessary, leading to a larger and more cumbersome actuation system. In response to these challenges, recent innovations have introduced advanced structures and actuators to improve the flexibility of continuum robots for medical application [15], [16]. Noteworthy developments

include an origami-inspired actuator designed for upper gastrointestinal endoscopy [17], ferromagnetic soft continuum robots for cerebral vascular aneurysm treatments [18], [19], and shape memory alloy (SMA)-actuated spring-based continuum robot for MRI-guided neurosurgery [20], [21]. These advancements demonstrate a concerted effort to refine the functionality and application of continuum robots in the medical field, addressing previous limitations related to flexibility and system size.

Besides, variable stiffness technologies of continuum robots have also attracted extensive attention for their potential to enhance surgical performance in confined spaces of the human body [22]. Specifically, lower stiffness at the tip (or the whole body) of the robot facilitates safe navigation in narrow spaces, while higher stiffness facilitates the manipulation ability for lesions. Currently, there are three primary methods to change the stiffness of the robot. The first is material-based stiffness adjustment. This approach involves filling the robot with materials that can alter stiffness in response to physical or chemical factors, such as LMPA [23] or shape memory polymer (SMP) [24], [25]. However, the process of changing stiffness with these materials can take time and effort. The second is internal friction changing. The friction of the internal components of the robot can be increased by particle [26] or layer jamming [27], leading to a greater force to deform. While effective, this method may lead to increased mechanical wear and a reduction in the robot's lifespan. The third is a structural configuration change. Typical examples are the continuum robots with pre-programmed tensegrity structure [28], or nonuniform patterns [29]. This approach often requires the robot to maintain a certain configuration and has limited flexibility.

In conclusion, to address the trade-offs between the limited flexibility of single-segment active bending continuum robots and the challenges in maintaining precise control over multi-segment functional bending robots, we propose a novel design: a variable-length single-segment active bending continuum robot. This design significantly expands the robot's operational space. Furthermore, by employing a combination of material-based and structure-based methods for adjusting stiffness, the robot can adopt various stiffness configurations to suit different in surgical tasks, enhancing its overall flexibility. At the algorithmic level, we have developed a stiffness model for the robot and designed a learning-based stiffness compensation algorithm. This algorithm is tailored to compensate for the errors induced by friction or gravity. Additionally, we have engineered a contact force controller specifically for ablation force control within the human body. These advancements collectively aim to refine the robot's performance, making it more adaptable and efficient for endoscopic surgical application, as depicted in Fig. 1. The main contributions of this paper can be summarized in the following three points:

- A variable-length single-segment active bending continuum robot with variable stiffness is proposed, which can achieve omnidirectional bending and axial elongation. The robot uses material solid-liquid transition and structural changes to adjust its stiffness.
- The stiffness model and a learning-based stiffness compensation approach of the variable-length continuum robot are proposed to establish the relationship between the robot stiffness, material properties, and driving force. In addition, a force controller is proposed for ablation surgery.
- The robot integrates a magnetic positioning sensor, a micro camera, and surgical tools and has been comprehensively validated in the in vitro experiments in a gastrointestinal model, confirming its surgical application potential.

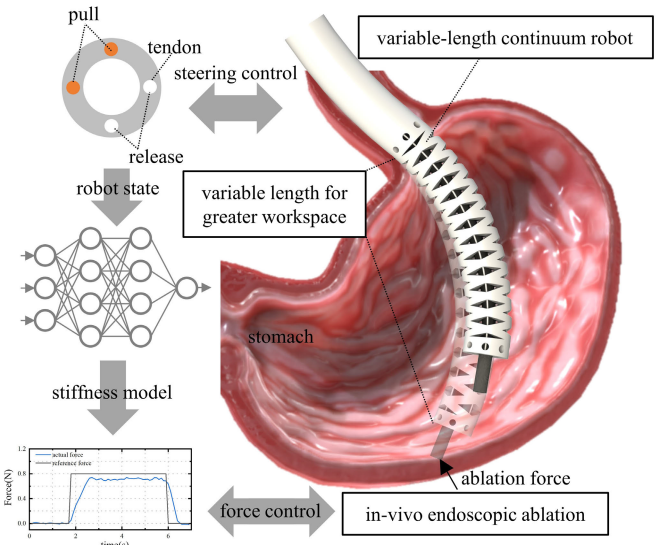

Fig. 1. Force control diagram of the variable-length continuum robot for endoscopic mucosal ablation. The robot is controlled to reach the target area, showing large workspace and high dexterity. During the ablation procedure, the neural network outputs the compensation to improve the accuracy of the stiffness model used for contact force control.

The article is organized as follows. In Section II, the design and fabrication of a quasi-static stiffness model, along with a learning-based stiffness compensation approach, are introduced. Besides, a contact force controller is proposed for ablation surgery. In Section III, the characterization experiment, variable stiffness analysis, force control experiment, and gastrointestinal surgical demonstration are carried out to assess the performance of the proposed robot comprehensively. In Section V, the main achievements and improvements of this work are briefly concluded.

II. Methods

A. Design and Fabrication

The design and fabrication of the variable-length continuum robot are depicted in Fig. 2(a). The robot mainly consists of a robotic arm to adjust the robot pose, a variable-length catheter with an outer diameter (OD) of 12.6 mm used for endoscopic surgery, and an actuation system to control the catheter. The catheter is designed to achieve omnidirectional steering and axial elongation under the actuation of the rod (made of Nitinol). The actuation system consists of four linear motors mounted on the motor fixture (Fig. 2(b)), which are used to pull the rod to steer or elongate the variable-length catheter. Each linear motor is installed with a force sensor through the motor flange and sensor connector, and the force

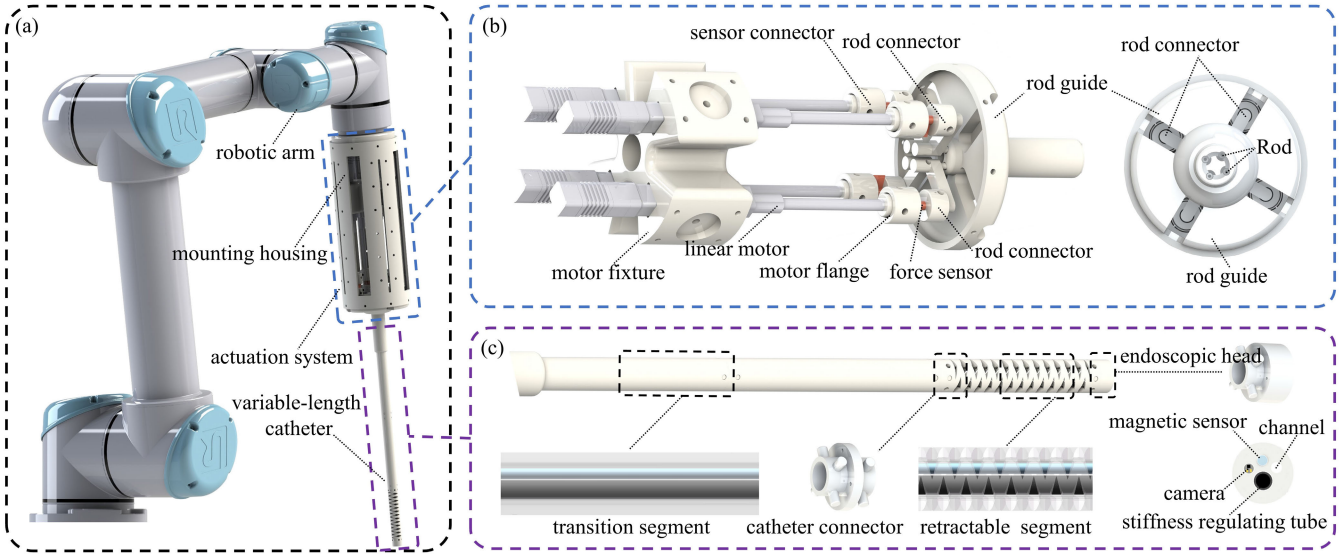

Fig. 2. The design and fabrication of the variable-length continuum robot. (a) The CAD model of the variable-length continuum robot. It consists of a robotic arm to adjust the robot pose, a variable-length catheter used for endoscopic surgery, and the actuation system for the shape control of the catheter. (b) The CAD model of the actuation system. It consists of four linear motors to pull the rods to steer or extend the variable-length catheter. Each linear motor is installed with a force sensor to measure the driving force. (c) The CAD model of the variable-length catheter. It mainly consists of a retractable segment and a transition segment used for passive compliance.

sensor connects with the rod through the rod connector. During movement, the force sensors are used to measure the driving force in real-time.

The detailed structure of the variable-length catheter is depicted in Fig. 2(c). It consists of a retractable segment used for steering or elongation control, a transition segment used for passive compliance, an endoscopic head used to install endoscopic equipment, and a catheter connector used to bond the retractable segment and transition segment. In this robot, a magnetic positioning sensor (610060, Northern Digital Inc., Canada), a micro camera (OCHTA10, OmniVision Technologies Inc., America), a working channel (made of polycarbonate), and a stiffness regulating tube (with an OD of 4mm) are installed on the endoscopic head. The transition and retractable segments are made of silicone materials but have different stiffnesses. Besides, the retractable segment has many triangle-shaped incisions, resulting in much lower stiffness than the transition segment.

The structure of the stiffness regulating tube is depicted in Fig. 3(a). It is filled with LMPA, wound with the heating wire (made of 0.1 mm copper wire), and then encapsulated by a TPU layer. It can adjust the stiffness of the variable-length catheter by switching the state of the LMPA (melt by heating and solidify by cooling). Additionally, the detailed fabrication of the retractable segment is also introduced, as depicted in Fig. 3(b). Firstly, two fluted parts (bottom and top) made of resin materials are closed to form a groove. Secondly, seal the fluted parts with one end cap and pour the liquid silica gel (Polydimethylsiloxane material) into the groove. When filled with liquid, put on the other end cap. Thirdly, insert the spindle and pins to form a working channel and four holes for placing the push rods. After high-temperature curing, the spindle, pins, end caps, and fluted parts are successively removed, and the retractable segment is obtained. Similarly, the transition segment can be fabricated by the same fabrication process.

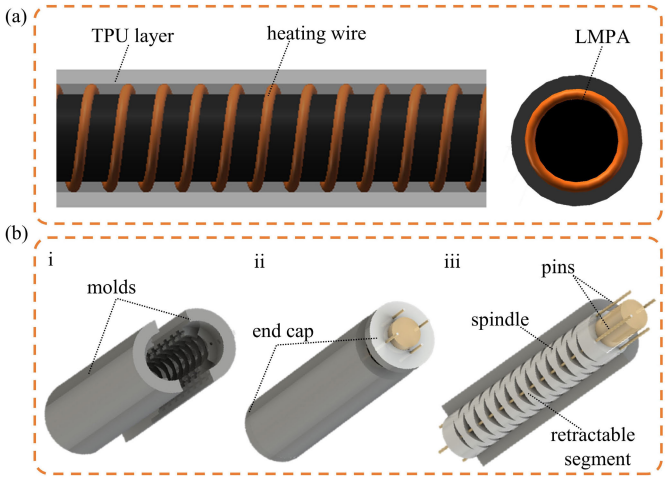

Fig. 3. The design and fabrication of stiffness regulating tube.(a) The CAD model of the stiffness regulating tube. (b) The detailed fabrication process for the variable-length catheter.

B. Kinematic Model

To analyze the movement of the variable-length catheter, the kinematic analysis is conducted, as shown in Fig. 3. The coordinate system $\{o_b x_b y_b z_b\}$ and $\{o_t x_t y_t z_t\}$ are established on the base and tip of the variable-length catheter. The coordinate system $\{o_{rt} x_{rt} y_{rt} z_{rt}\}$ and $\{o_{rb} x_{rb} y_{rb} z_{rb}\}$ are established on the tip and base of the retractable segment. Four tendons are fixed on the catheter tip and run parallel to the centroidal axis of the catheter at a radius d.

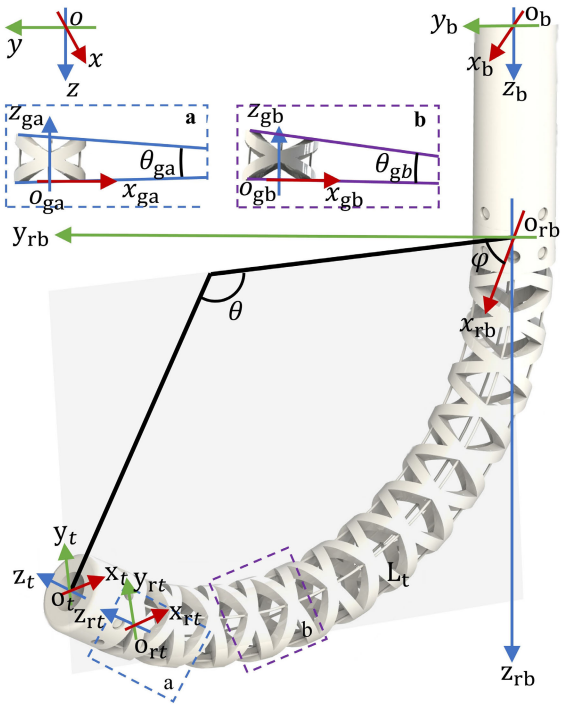

Fig. 4. Kinematic schematic diagram of the variable-length catheter.

To simplify the kinematic model, assume that the retractable segment deforms in constant curvature [30], [31] under the actuation of the rods. As depicted in Fig. 4, the configuration parameters include the bending angle θ, bending plane angle φ and the length L_t (initial length L_0), relative to the coordinate system $\{o_{rb}x_{rb}y_{rb}z_{rb}\}$. The retractable segment has N triangle-shaped incisions in vertical directions respectively. We have

$$\theta_{ga} = \frac{1}{\mathrm{N}}\theta\cos(\varphi) \tag{1}$$

$$\theta_{gb} = \frac{1}{\mathrm{N}}\theta\sin(\varphi) \tag{2}$$

The transformation matrix ${}^{t}_{b}\mathbf{T}$ between the catheter base and the tip can be represented as follows.

$${}^{t}_{b}\mathbf{T} = {}^{rb}_{b}\mathbf{T}\cdot{}^{rt}_{rb}\mathbf{T}\cdot{}^{t}_{rt}\mathbf{T} = {}^{rb}_{b}\mathbf{T}\cdot\begin{bmatrix}{}^{rt}_{rb}\mathbf{R} & {}^{rt}_{rb}\boldsymbol{p}\\ 0 & 1\end{bmatrix}\cdot{}^{t}_{rt}\mathbf{T} \tag{3}$$

where ${}^{rb}_{b}\mathbf{T}$ and ${}^{rt}_{rb}\mathbf{T}$ are respectively the transformation matrix from the base to tip of the transition segment and retractable segment. ${}^{rt}_{rb}\mathbf{R}$ and ${}^{rt}_{rb}\boldsymbol{p}$ are respectively the rotation matrix and position vector. We have

$${}^{t}_{b}\boldsymbol{p} = {}^{rb}_{b}\boldsymbol{p} + {}^{rb}_{b}\mathbf{R}\cdot{}^{rt}_{rb}\boldsymbol{p} + {}^{rb}_{b}\mathbf{R}\cdot{}^{rt}_{rb}\mathbf{R}\cdot{}^{t}_{rt}\boldsymbol{p} \tag{4}$$

$${}^{t}_{b}\mathbf{R} = {}^{rb}_{b}\mathbf{R}\cdot{}^{rt}_{rb}\mathbf{R}\cdot{}^{t}_{rt}\boldsymbol{R} \tag{5}$$

where ${}^{t}_{rt}\boldsymbol{p} = [0, 0, \mathrm{h}]^{\mathrm{T}}$, and h is the length of the catheter tip. By deploying sensors on the catheter, the parameters of the above equations can be obtained in real time. Based on the constant curvature assumption, ${}^{rt}_{rb}\mathbf{R}$ and ${}^{rb}_{rb}\boldsymbol{p}$ could be solved by the parameters L_t, θ, and φ as follows.

$${}^{rt}_{rb}\boldsymbol{p} = \frac{L_t}{\theta}\begin{bmatrix}\mathrm{c}_\varphi(\mathrm{s}_\theta - 1)\\ -\mathrm{s}_\varphi(\mathrm{s}_\theta - 1)\\ -\mathrm{c}_\theta\end{bmatrix} \tag{6}$$

$${}^{rt}_{\mathrm{rb}}\mathbf{R} = e^{-\varphi[\hat{\mathbf{w}}\times]}e^{-\theta[\hat{\mathbf{v}}\times]}e^{\varphi[\hat{\mathbf{w}}\times]} \tag{7}$$

where s_α and c_α are abbreviated form of the cosine and sine, respectively $\mathrm{s}_\alpha = \sin\alpha$, $\mathrm{c}_\alpha = \cos\alpha$, and $\hat{\mathbf{v}} = [0, 1, 0]^{\mathrm{T}}$, $\hat{\mathbf{w}} = [0, 0, 1]^{\mathrm{T}}$

Define the actuation state $\boldsymbol{q}$ as

$$\boldsymbol{q} = [L_1, L_2, L_3, L_4]^{\mathrm{T}} \tag{8}$$

where $L_i, i = 1, \ldots, 4$ is tendon displacement. We have

$$L_i = -L_c + d\theta\cos(\alpha_i), i = 1, \ldots, 4 \tag{9}$$

where L_c is the extension length of the retractable segment and α_i is defined as

$$\alpha_i = \varphi - \pi\frac{i-1}{2} \tag{10}$$

The twist $\boldsymbol{t}$ of the retractable segment can be obtained by the rate of change of the configurations state $\dot{\boldsymbol{\psi}} = [\dot{\theta}, \dot{\varphi}, \dot{L_c}]$, and the rate of change of the actuation state $\dot{\boldsymbol{q}}$, as

$$\boldsymbol{t} = \mathbf{J}_{t\psi}\dot{\boldsymbol{\psi}} \tag{11}$$

$$\dot{\boldsymbol{q}} = \mathbf{J}_{q\psi}\dot{\boldsymbol{\psi}} \tag{12}$$

where $\mathbf{J}_{t\psi}$ is the geometric Jacobian relating configuration space and task space velocities, while $\mathbf{J}_{q\psi}$ is the Jacobian relating configuration space and joint space velocities [32].

C. Stiffness Model

During motion control, the retractable segment would steer or elongate actively under the actuation of the rods, while the transition segment passively deforms. In instantaneous time, only the potential energy variation of the retractable segment, along with the driving rods, is considered. Neglecting gravity [33], the potential energy consists of the bending energy U_b and axial compression energy U_c, then the potential energy U_b can be defined using Euler-Bernoulli beam element analysis as

$$\begin{aligned}\mathrm{U}_b =& \frac{1}{2}\mathrm{NEI}\int_0^{\frac{L_t}{2\mathrm{N}}}\left(\frac{d\theta_{pa}}{ds}\right)^2 + \left(\frac{d\theta_{pb}}{ds}\right)^2 ds\\ &+ \sum_{i=1}^{4}\frac{1}{2}\mathrm{E}_r\mathrm{I}_r\int_0^{L_i}\left(\frac{d\theta_{pi}}{ds}\right)^2 ds\\ =& \frac{1}{2}\frac{\mathrm{EI}}{L_t}\theta^2 + \frac{1}{2}\sum_{i=1}^{4}\frac{\mathrm{E}_r\mathrm{I}_r}{L_i}\theta^2\end{aligned} \tag{13}$$

where L_t is the current length of the retractable segment. E, I, and $\mathrm{E}_r, \mathrm{I}_r$ are, respectively, Young's modulus, area moment of inertia of the retractable segment, and the push rod. θ_{pa}, θ_{pb} are respectively the bending angle of any point along the length of the triangle-shaped incisions, while θ_{pi} is the bending angle of any point along the length of the i-th rod. We have

$$\theta_{pa} = s\frac{2\mathrm{N}\theta_{ga}}{L_t}$$

$$\theta_{pb} = s\frac{2\mathrm{N}\theta_{gb}}{L_t}$$
$$\theta_{pi} = s\frac{\theta}{L_i} \tag{14}$$

where s is the distance of the point to the base along the centerline. The potential energy due to the axial extension of the retractable segment can be derived by

$$U_c = \frac{1}{2}\mathrm{EA}\int_0^{\mathrm{L}_0}\left(\frac{du_p}{ds}\right)^2 ds = \frac{1}{2}\frac{\mathrm{EA}}{\mathrm{L}_0}(L_t - \mathrm{L}_0)^2 \tag{15}$$

where A, and $u_p = s\frac{L_t - \mathrm{L}_0}{\mathrm{L}_0}$ are the cross-section area of the retractable segment and the axial extension of any point $\boldsymbol{p}$ along the length of the segment, respectively. Thus, the total potential energy U can be represented as

$$\mathrm{U} = \mathrm{U}_b + \mathrm{U}_c \tag{16}$$

The generalized force perturbation $\delta\mathbf{f}_\psi$ associated with the retractable segment with respect to its configuration space perturbation $\delta\boldsymbol{\psi}$ is described as follows.

$$\delta \boldsymbol{f}_\psi = \mathbf{K}_\psi \delta\boldsymbol{\psi} \tag{17}$$

where $\mathbf{K}_\psi$ is the stiffness matrix. The elements of $\mathbf{K}_\psi$ can be solved [34] as follows.

$$\mathbf{K}_\psi = \frac{\partial}{\delta\boldsymbol{\psi}}\left[\nabla \mathrm{U} - \mathbf{J}_{q\psi}^{\mathrm{T}}\boldsymbol{\tau}\right] \tag{18}$$

where $\boldsymbol{\tau}$ represents the actuation force state.

The wrench acting on the tip of the retractable segment can be projected by the generalized force as follows.

$$\boldsymbol{f}_\psi = \mathbf{J}_{t\psi}^{\mathrm{T}}\mathbf{w} \tag{19}$$

D. MLNN-Based Stiffness Compensation

In the above section, due to the neglected gravitational potential energy, fabrication, and assembly errors, and the frictions between the rods and the catheter, along with the unconsidered variation of elastic modulus during elongation of the catheter, there might result in a deviation $\mathbf{K}_\varepsilon$ of the stiffness model. Thus, the actual stiffness matrix takes the form.

$$\widehat{\mathbf{K}}_\psi = \mathbf{K}_\psi + \mathbf{K}_\varepsilon \tag{20}$$

To compensate for the stiffness matrix, a multi-layer neural network (MLNN) is used to establish a stiffness compensation function h_ε. The MLNN consists of an input layer, two hidden layers, and an output layer. Each hidden layer is composed of a fully connected layer (with 50 neurons) with the Rectified Linear Unit activation function and a BatchNorm layer to standardize the outputs. The actuation state $\boldsymbol{q}$ can be implicitly expressed by the configuration states $\boldsymbol{\psi}$ and its derivative $\dot{\boldsymbol{\psi}}$, thus the input $\mathbf{I}_\varepsilon$ of the MLNN can be represented as follows.

$$\mathbf{I}_\varepsilon = \left[\,\dot{\boldsymbol{\psi}}^{\mathrm{T}}\ \boldsymbol{\psi}^{\mathrm{T}}\ \boldsymbol{\tau}\,\right]^{\mathrm{T}} \tag{21}$$

The output of the MLNN is the systematic deviation $\mathbf{K}_\varepsilon$, could be represented by

$$\mathbf{K}_\varepsilon = h_\varepsilon(\mathbf{I}_\varepsilon) \tag{22}$$

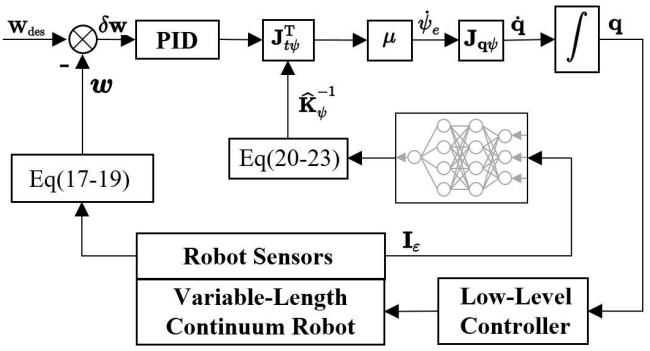

Fig. 5. Force controller for the variable-length continuum robot.

Define the loss function $l_c(\mathbf{I}_\varepsilon, \boldsymbol{q})$ as follows

$$l_c(\mathbf{I}_\varepsilon, \boldsymbol{q}) = \left|\mathbf{J}_{\mathbf{t}\psi}\left(\mathbf{K}_\psi + \mathbf{K}_\varepsilon\right)\dot{\boldsymbol{\psi}} - \delta\mathbf{w}\right| \tag{23}$$

where $\delta\mathbf{w}$ is the external force perturbation. $\mathbf{K}_\psi$ is the solved stiffness matrix by equation (18), and $\mathbf{K}_\varepsilon$ is the compensation matrix outputted by MLNN. During the training process, the Adam solver is used to minimize the loss function and optimize the network parameters. The learning rate is set as 0.001, and the early stopping technique is applied to avoid overfitting. To collect sufficient data, we discretized sampling within the interval of each configuration parameter: 10 points were discretized for bending angle, 36 points for bending plane angle, and 10 points were discretized for elongation. Due to the strong nonlinear fitting ability of neural networks, the predictive stiffness of any configuration can be obtained based on the trained neural networks.

E. Contact Force Controller

During endoscopic surgery, particularly during ablation procedures, it's crucial for the catheter tip to contact with the tissue while maintaining a stable force. Thus, based on the proposed stiffness model, a force controller is proposed for the variable-length catheter. Define the desired force as $\mathbf{w}_{\mathrm{des}}$, we have

$$\delta\mathbf{w} = \mathbf{K}_p(\boldsymbol{e}_n - \boldsymbol{e}_{n-1}) + \mathbf{K}_i\boldsymbol{e}_n + \mathbf{K}_d(\boldsymbol{e}_n - 2\boldsymbol{e}_{n-1} + \boldsymbol{e}_{n-2}) \tag{24}$$

where $\boldsymbol{e} = \mathbf{w}_{des} - \mathbf{w}$, $\boldsymbol{e}_n$ is the force error at step n, and $\boldsymbol{w}$ is the external force. $\mathbf{K}_p$, $\mathbf{K}_i$ and $\mathbf{K}_d$ are respectively the proportional, integral, and differential coefficient matrix. Thus, the control law could be written as

$$\dot{\boldsymbol{\psi}}_e = \mu\widehat{\mathbf{K}}_\psi^{-1}\mathbf{J}_{t\psi}^{\mathrm{T}}\delta\mathbf{w} \tag{25}$$

where μ is the adjustment coefficient, and $\dot{\boldsymbol{\psi}}_e$ is the desired configuration space velocity vector.

Based on the proposed control law, the force controller is designed as depicted in Fig. 5. The force error $\boldsymbol{e}$ is calculated by the estimated external force $\mathbf{w}$ and the desired force $\mathbf{w}_{des}$. After amplified by the incremental PID coefficients, it is converted into the configuration space velocity vector $\dot{\boldsymbol{\psi}}_e$ and transferred to the actuation state $\boldsymbol{q}$. By the low-level controller, the variable-length continuum robot reaches the desired force.

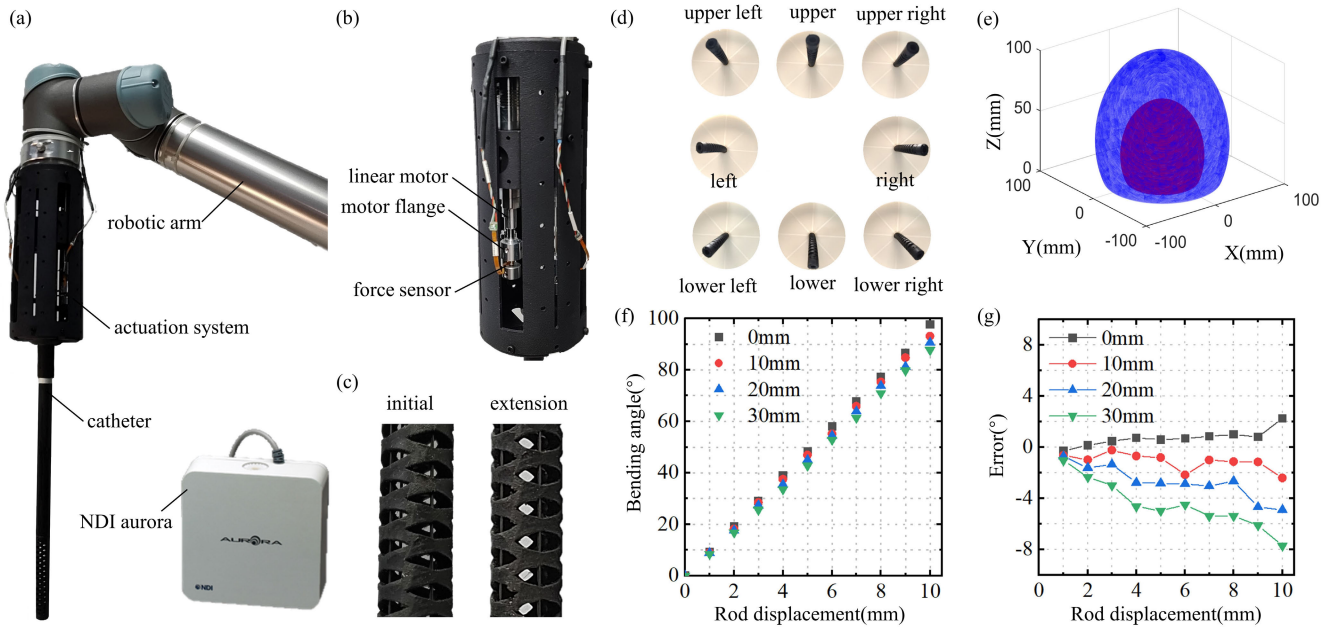

Fig. 6. Characterization experiments of the variable-length continuum robot. (a) Hardware system integration. (b) The integration of the actuation system. (c) The catheter structure before and after elongation. (d) Steering experiment. (e) Workspace analysis. (f) The relationship between the driving displacement and the bending angle of the retractable segment under 0mm, 10mm, 20mm, and 30mm elongations. (g) The bending angle error under 0mm, 10mm, 20mm, and 30mm elongations.

III. Results

A. Characterization Experiments

To assess the performance of the proposed variable-length continuum robot, the experimental system is integrated, as shown in Fig. 6(a). This system includes a robotic arm for pose adjustment, a variable-length continuum robot for endoscopic surgery, and a magnetic positioning sensor to track the pose of the catheter tip. Fig. 6(b) shows the integration of the actuation system. It includes four linear motors dedicated to steering or elongating the catheter alongside four force sensors tasked with measuring the driving force. The catheter structure before and after elongation is shown in Fig. 6(c).

To evaluate the robot's maneuverability, an active steering experiment was conducted, as depicted in Fig. 6(d). The experiment's snapshots reveal the catheter bending in eight directions, driven by the rods, with an elongation of 30mm (maximum elongation). This demonstrates the catheter's good steering capabilities, as the orientation of the catheter closely aligns with the direction of the notch on the base. In addition, the robot's workspace before and after the elongation is plotted in Fig. 6(e). The red scatter points represent the area reachable by the catheter tip before elongation, whereas the blue scatter points depict the expanded reachable region following a 30mm elongation. The area between these two points indicates the enhanced accessible region for the variable-length catheter. These experimental results unequivocally show that the variable-length catheter boasts an expanded workspace and superior flexibility.

Next, kinematic characterization experiments are carried out to verify the model accuracy for the continuum robot. Fig. 6(f) depicts the relationship between the rod displacement and the bending angle of the retractable segment under 0mm, 10mm, 20mm, and 30mm elongations. The results demonstrated a linear relationship between the rods' driving displacement and the retractable segment's bending angle, confirming the linear behavior predicted by the kinematic model. The scatter points representing the bending angle at different elongations closely overlapped, indicating that the robot's behavior remains consistent across different lengths of elongation and aligns well with the proposed kinematic model. Fig. 6(g) depicts the error variation under 0mm, 10mm, 20mm, and 30mm elongations. It can be seen that as the elongation increases, the error in the model's predictions gradually rises. The main reason is that elongating the catheter by applying force through the rods introduces additional stresses within the catheter structure. These stresses lead to increased friction between the rod and the catheter, which, in turn, impacts the model's accuracy. The phenomenon demonstrates the complexity of accurately modeling the behavior of continuum robots, especially when considering the dynamic interactions between mechanical components under stress.

To evaluate the control accuracy of the robot, a trajectory tracking experiment is carried out. The catheter tip is controlled to move along a circle based on the proposed kinematic model, while the magnetic positioning sensor is used to record the actual trajectory. Fig. 7(a) and (b) respectively show the real and ideal trajectory points projected on the XY plane and XZ plane. It is observed that the two trajectories have a reasonable degree of overlap in most directions, but there are some differences in specific directions. By calculation, the average position error is 1.78 mm (4.45% relative to the radius of 40 mm), and the maximum position error is 3.91 mm. Overall, the tracking error still fluctuates within a controllable

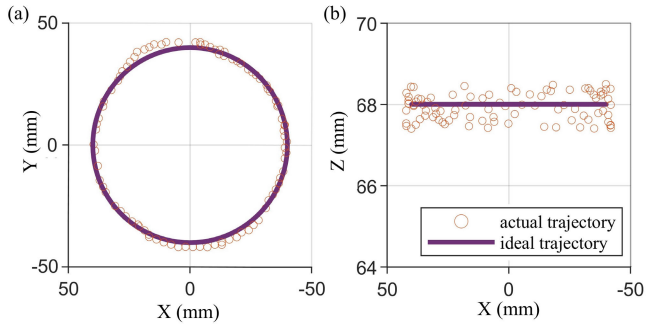

Fig. 7. Trajectory tracking experiments. (a) The actual and ideal trajectory points projected on the XY plane. (b) The actual and ideal trajectory points projected on the XZ plane.

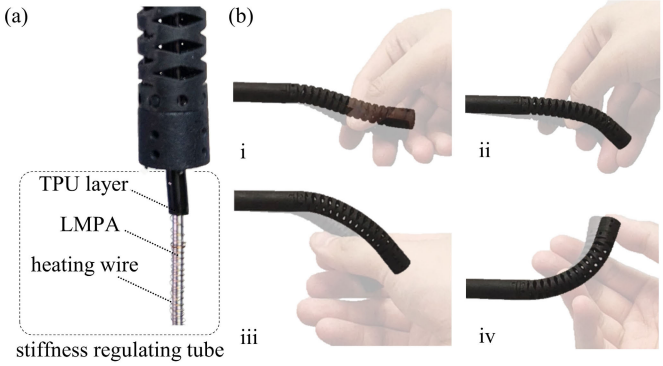

Fig. 8. Catheter shaping experiment. (a) Integration of the variable-length catheter with variable stiffness. (b) Snapshots of the catheter shaping experiment.

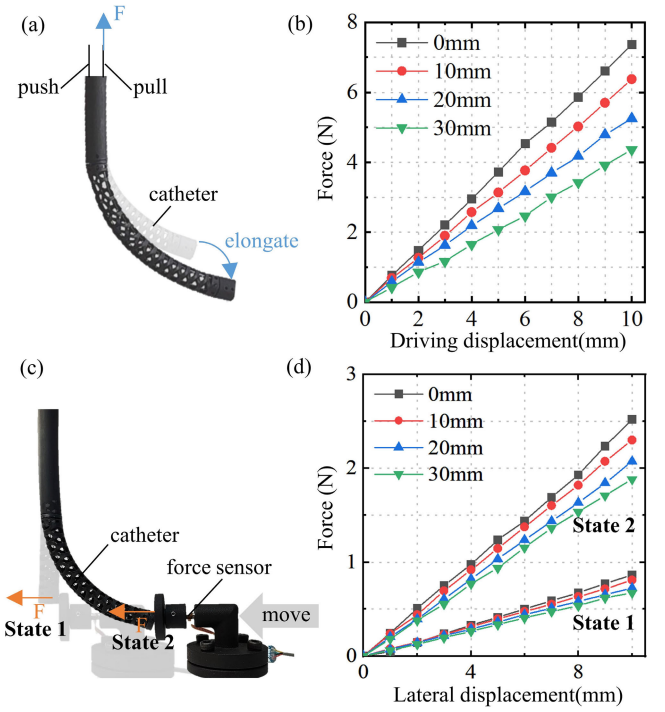

Fig. 9. Variable stiffness analysis under different elongations.(a) Steering control diagram under different elongations. (b) Force-driving displacement relationship under different elongations. (c) Experimental setting of lateral stiffness measurement. (d) Force-lateral displacement relationship under two configurations.

range, showing the good open control performance of the proposed controller.

B. Variable Stiffness Analysis

To validate the catheter's variable stiffness capability, enabled by the solid-liquid transition of Low Melting Point Alloy (LMPA), a catheter shaping experiment is conducted. Initially, LMPA (with a melting point of 47 degrees Celsius) is cooled to a solid state and encased within a Thermoplastic Polyurethane (TPU) layer, forming the stiffness-regulating tube. This tube is then integrated into the variable-length catheter, with its tip securely attached (Fig. 8(a)). During the experiment, the catheter's shape is manually altered and subsequently released, showcasing the catheter's ability to maintain any given configuration post-manipulation (Fig. 8(b)). The comparison of translucent (before release) and opaque (after shaping) images illustrates the catheter's capacity to hold a stable shape once the LMPA solidifies. This feature is particularly beneficial for ensuring stability when surgical tools are inserted into the catheter.

Next, the variable stiffness capability of the catheter, enabled by the changes in its length, is tested by controlling the catheter to steer at varying elongations, as depicted in Fig. 9(a). The relationship between driving force and driving displacement is plotted in Fig. 9(b). The purple, red, blue, and green curves, respectively, represent the curves under 0mm, 10mm, 20mm, and 30mm elongations. It is observed that with the increase of elongation, the driving force under the same driving displacement decreases. This decrease is attributed to the reduction in deformation per unit length after elongation, thereby lowering the stress and required driving force. Notably, the consistency across the relationship curves for all four elongations suggests uniform material and mechanical properties of the catheter in all directions. Additionally, the catheter's lateral stiffness is analyzed by controlling it to respectively maintain axial deformation and the same unilateral steering at different elongations, with a force sensor measuring the lateral stiffness (see Fig. 9(c)). The relationship between the lateral displacement and force is plotted in Fig. 9(d). It is observed that the lateral stiffness diminishes as elongation increases, and notably, the lateral stiffness after bending significantly exceeds that observed during mere elongation. The main reason is that the driving force of the rod increases when bending, which increases the stress distribution of the catheter and changes its transverse stiffness. The above experiments fully verify the variable stiffness ability of the catheter after length changes and material solid-liquid transition.

C. Force Control Experiment on Stomach Model

To test the force control accuracy of the variable-length continuum robot, force tracking experiments are carried out, as depicted in Fig. 10(a). The catheter equipped with an ablation probe on its tip is controlled to apply force to the force measurement platform installed with a force sensor, following triangle and sinusoidal reference forces. The control frequency of the robot is set as 50Hz. Two trials of actual force and

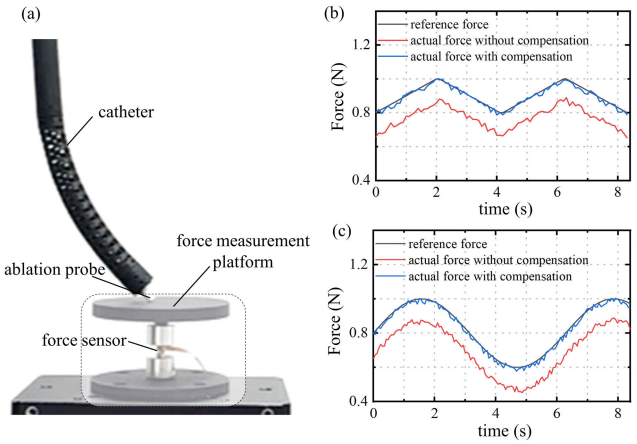

Fig. 10. Force tracking experiment. (a) The experimental setup. (b) The tracking force and reference triangle force variation curves. (c) The tracking force and reference sinusoidal force variation curves.

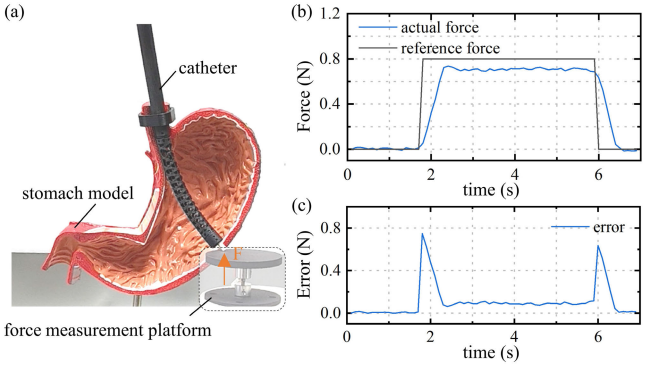

Fig. 11. Ablation force control experiment. (a) The experimental setup. (b) The actual force and reference force variation curves (c) The force error variation curve.

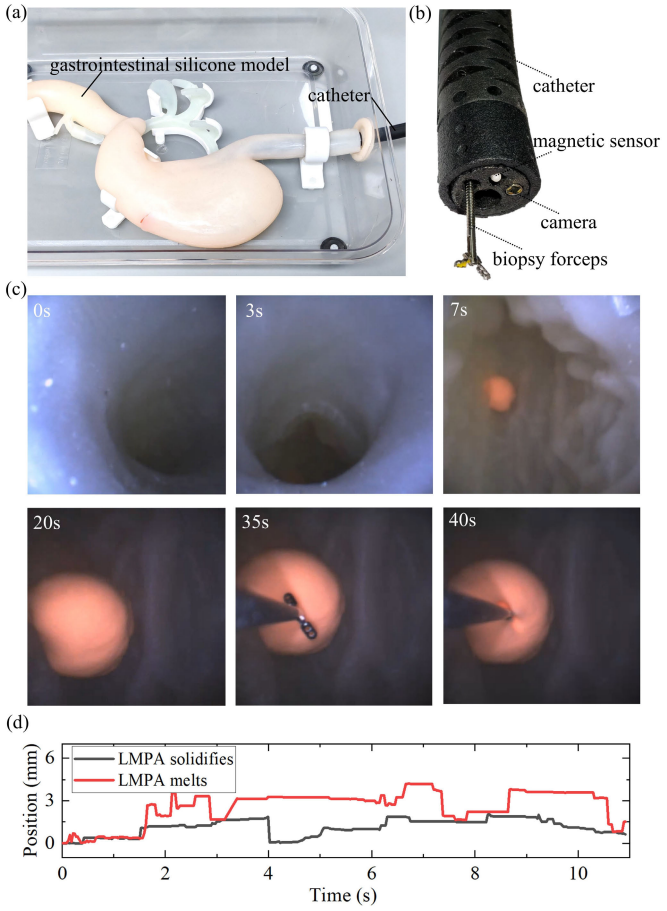

Fig. 12. Gastrointestinal surgical demonstration. (a) The experimental scene. (b) The catheter integrated with a working channel and a micro camera. (c) Snapshots of surgical process in the gastrointestinal model. (d) The changes in position of the catheter tip when performing tissue sampling with LMPA in a solid versus a liquid state.

reference force are plotted in Fig. 10(b) and (c). Notably, there is a certain deviation between the actual force without stiffness compensation and the reference force. However, with stiffness compensation, the actual forces are closely aligned with the reference forces, significantly improving tracking performance. The mean errors of the two signals without compensation are 133 mN and 129 mN for the triangle and sinusoidal signals, respectively, but dropped to 21 mN and 23 mN with compensation. The results demonstrate the force controller's high accuracy and the substantial impact of stiffness compensation on enhancing force-tracking capabilities in surgical applications.

To demonstrate the robot's potential in endoscopic surgery, an ablation force control experiment is carried out, as depicted in Fig. 11(a). The variable-length catheter, equipped with an ablation probe, is controlled to insert into the stomach model to simulate a surgical procedure. Due to the ample workspace and high flexibility, it can reach most areas of the stomach model. Upon making contact with the force measuring platform (mimic lesion tissues), an ablation force control task is initiated with a set desired force of 0.8 N. It can be seen from Fig. 11(b) that the catheter quickly achieved the target force. However, the contacts between the catheter body and the stomach model introduced challenges, diminishing the stiffness model's accuracy and leading to the deviation between the actual and the desired forces. Fig. 11(c) shows the error variation during the experiment. It can be seen that the force error is particularly noticeable during the rise and fall phases, with a mean error of about 0.09 N throughout the process. The experiment highlighted the robot's potential to perform endoscopic surgery in confined spaces.

D. Gastrointestinal Surgical Demonstration

To further demonstrate the endoscopic surgical capability of the robot, a tissue sampling experiment is conducted in a gastrointestinal model, as depicted in Fig. 12(a). The variable-length catheter, equipped with a working channel, a magnetic sensor and a micro camera, allows for the insertion of surgical tools, such as biopsy forceps (see Fig. 12(b)). During the experiment, the LMPA is initially heated for about 15s (the heating wire is applied to a voltage of 10V) to change into a liquid state, at this time, the catheter has low stiffness, and can be controlled to locate the lesion (simulated by a silly putty ball) within the gastrointestinal model. Upon identifying a lesion, the catheter's tip is precisely directed toward the target area, followed by the solidification of the LPMA (cool for about 10s) within the catheter to enhance its stiffness for

TABLE I
COMPARISON BETWEEN THIS WORK AND THE OTHER STUDIES

Ref	Actuation	Dimension	Variable stiffness principle	Variable length	Control frequency	Application
[26]	pneumatic	⌀30 mm	granular jamming	no	-	minimally invasive surgery
[29]	tube-driven	⌀1.8 mm	nonuniform tubes movement	yes	-	steerable needle
[35]	tendon-driven	⌀15 mm	material glass transition	no	-	endoscopic manipulator
[36]	magnetic driven	⌀1 mm	material solid-liquid transition	no	10 Hz	ophthalmic surgery
[37]	pneumatic/cable-driven	⌀18 mm	pressure-based jamming	no	1000 Hz	gastrointestinal endoscopy
[38]	tendon-driven	⌀14.5 mm	fiber jamming	no	-	surgical manipulator
[39]	pneumatic	⌀3.6-21 mm	sandpaper jamming	no	-	endoscopic surgery
[40]	rod-driven	⌀8 mm	tube-based mechanism	no	-	transoral Surgery
[41]	magnetic driven	10×2 mm	sliding nitinol backbone	no	1 Hz	gastric surgery
[42]	magnetic driven	⌀0.8 mm	tube length adjustment	yes	130 Hz	coronary intervention
[43]	tube-driven	⌀8 mm	temperature changes of SMA and length changes	yes	-	transoral robotic surgery
ours	**rod-driven**	**⌀12.6 mm**	**material solid-liquid transition and length changes**	**yes**	**50 Hz**	**endoscopic surgery**

stable surgical intervention. Subsequently, the biopsy forceps is inserted through the working channel to carry out the surgical task, as shown in Fig. 12(c).

To demonstrate the benefits of variable stiffness capability, the changes in position of the catheter tip are compared when performing tissue sampling with LMPA in a solid versus a liquid state, as depicted in Fig. 12(d). The average position change is 1.1mm when LMPA solidifies, while that is 2.6mm when LMPA melts. It is observed that the solidification of LMPA improves the stiffness of the catheter, reduces the disturbance of the surgical tool during procedures, and increases the stability of the surgical process. This experiment showcases the robot's potential to significantly impact endoscopic surgical practices by enabling precise, flexible, and controlled interventions in complex anatomical regions.

IV. DISCUSSION AND CONCLUSION

This paper proposed a variable-length continuum robot with variable stiffness for endoscopic surgery. The robot can bend omnidirectionally and elongate along its axis under the actuation of the rods. Compared with the continuum robots with one active bending segment, the robot has higher flexibility and accessibility. Besides, a quasi-static stiffness model and a learning-based stiffness compensation approach are proposed for accurate stiffness estimation; then, a model-based force controller is designed for ablation surgery. According to the experimental results, the robot shows high flexibility, accessibility, and good force control accuracy.

To more comprehensively highlight the advantages of the work in this paper, we summarized the variable-stiffness surgical continuum robots that have been developed, as shown in Table I. Due to their large load capacity, most existing surgical robots adopt tendon-driven or pneumatic methods. For miniaturizing the robots, magnetic and tube-driven methods have also been adopted, with concentric tube robots being a subset of tube-driven designs. The prevalent robots adopt material-based (glass transition) or Jamming-based approaches to achieve variable stiffness. A few robots employ the structure-based approaches, such as the tube relative movement. Despite these varied approaches, the paper highlights a notable gap: few robots can simultaneously adjust their length and stiffness in real time, a capability integral to enhancing surgical precision and adaptability. The existing approaches to achieve variable length generally adopt a structure similar to that of the concentric tube robots, relying on the elongation of the backbone. Our robot uses the deformation of the hollow structure of the catheter to achieve the variable length capacity, and depends on the length change and the solid-liquid transition of LMPA to change the stiffness, marking a significant step forward in developing surgical continuum robots by combining online length variability with variable stiffness functionality.

However, it is worth noting that the retractable segment of the catheter is complicated and challenging to manufacture, and there are some differences in the material properties of the formed segments, reducing the model accuracy. Furthermore, the increase in the catheter's elongation also reduces the robot model's accuracy. It is worth studying to develop more accurate mechanical models for high-precision control of robots in the future.

REFERENCES

[1] G. Qin et al., "A snake-inspired layer-driven continuum robot," *Soft Robot.*, vol. 9, no. 4, pp. 788–797, Aug. 2022.
[2] J. Zhang et al., "A preprogrammable continuum robot inspired by elephant trunk for dexterous manipulation," *Soft Robot.*, vol. 10, no. 3, pp. 636–646, Jun. 2023.
[3] F. Meder, S. P. Murali Babu, and B. Mazzolai, "A plant tendril-like soft robot that grasps and anchors by exploiting its material arrangement," *IEEE Robot. Autom. Lett.*, vol. 7, no. 2, pp. 5191–5197, Apr. 2022.
[4] J. Zhang et al., "A survey on design, actuation, modeling, and control of continuum robot," *Cyborg Bionic Syst.*, vol. 2022, pp. 1–12, Jan. 2022.
[5] J. Burgner-Kahrs, D. C. Rucker, and H. Choset, "Continuum robots for medical applications: A survey," *IEEE Trans. Robot.*, vol. 31, no. 6, pp. 1261–1280, Dec. 2015.
[6] X. Zhang et al., "Robotic actuation and control of a catheter for structural intervention cardiology," in *Proc. IEEE/RSJ Int. Conf. Intell. Robots Syst. (IROS)*, 2022, pp. 5907–5913.
[7] M. A. Zenati and M. Mahvash, "Robotic systems for cardiovascular interventions," in *Medical Robotics*. Amsterdam, The Netherlands: Elsevier, 2012, pp. 78–89.
[8] J. Zhang et al., "AI co-pilot bronchoscope robot," *Nature Commun.*, vol. 15, no. 1, p. 241, Jan. 2024.
[9] X. Duan et al., "A novel robotic bronchoscope system for navigation and biopsy of pulmonary lesions," *Cyborg Bionic Syst.*, vol. 4, p. 0013, Jan. 2023.

[10] A. Bajo, R. B. Pickens, S. Duke. Herrell, and N. Simaan, "Constrained motion control of multisegment continuum robots for transurethral bladder resection and surveillance," in *Proc. IEEE Int. Conf. Robot. Autom.*, May 2013, pp. 5837–5842.
[11] W. Hong, F. Feng, L. Xie, and G.-Z. Yang, "A two-segment continuum robot with piecewise stiffness for maxillary sinus surgery and its decoupling method," *IEEE/ASME Trans. Mechatronics*, vol. 27, no. 6, pp. 4440–4450, Dec. 2022.
[12] F. Wang et al., "FIORA : A flexible tendon-driven continuum manipulator for laparoscopic surgery," *IEEE Robot. Autom. Lett.*, vol. 7, no. 2, pp. 1166–1173, Apr. 2022.
[13] W. Zeng, J. Yan, X. Huang, and S. Shin Cheng, "Motion coupling analysis for the decoupled design of a two-segment notched continuum robot," in *Proc. IEEE Int. Conf. Robot. Autom. (ICRA)*, May 2021, pp. 7665–7671.
[14] C. Girerd and T. K. Morimoto, "Design and control of a hand-held concentric tube robot for minimally invasive surgery," *IEEE Trans. Robot.*, vol. 37, no. 4, pp. 1022–1038, Aug. 2021.
[15] D. Liu et al., "Magnetically driven soft continuum microrobot for intravascular operations in microscale," *Cyborg Bionic Syst.*, vol. 2022, Jan. 2022, Art. no. 9850832.
[16] J. Liu, T. Xu, and X. Wu, "Model predictive control of magnetic helical swimmers in two-dimensional plane," *IEEE Trans. Autom. Sci. Eng.*, vol. 21, no. 2, pp. 1–10, Apr. 2024.
[17] M. Chauhan, J. H. Chandler, A. Jha, V. Subramaniam, K. L. Obstein, and P. Valdastri, "An origami-based soft robotic actuator for upper gastrointestinal endoscopic applications," *Frontiers Robot. AI*, vol. 8, pp. 1–12, May 2021.
[18] Y. Kim, G. A. Parada, S. Liu, and X. Zhao, "Ferromagnetic soft continuum robots," *Sci. Robot.*, vol. 4, no. 33, pp. 1–10, Aug. 2019.
[19] Y. Kim et al., "Telerobotic neurovascular interventions with magnetic manipulation," *Sci. Robot.*, vol. 7, no. 65, Apr. 2022, Art. no. eabg9907.
[20] Y. Kim, S. S. Cheng, M. Diakite, R. P. Gullapalli, J. M. Simard, and J. P. Desai, "Toward the development of a flexible mesoscale MRI-compatible neurosurgical continuum robot," *IEEE Trans. Robot.*, vol. 33, no. 6, pp. 1386–1397, Dec. 2017.
[21] S. S. Cheng, Y. Kim, and J. P. Desai, *Towards Real-Time SMA Control for a Neurosurgical Robot: MINIR-II*. Springer, 2018, pp. 187–200.
[22] Y. Zhong, L. Hu, and Y. Xu, "Recent advances in design and actuation of continuum robots for medical applications," *Actuators*, vol. 9, no. 4, p. 142, Dec. 2020.
[23] Y. Hao, J. Gao, Y. Lv, and J. Liu, "Low melting point alloys enabled stiffness tunable advanced materials," *Adv. Funct. Mater.*, vol. 32, no. 25, Jun. 2022, Art. no. 2201942.
[24] M. Mattmann et al., "Thermoset shape memory polymer variable stiffness 4D robotic catheters," *Adv. Sci.*, vol. 9, no. 1, Jan. 2022, Art. no. 2103277.
[25] J. Delaey, P. Dubruel, and S. Van Vlierberghe, "Shape-memory polymers for biomedical applications," *Adv. Funct. Mater.*, vol. 30, no. 44, 2020, Art. no. 1909047.
[26] I. De Falco, M. Cianchetti, and A. Menciassi, "A soft multi-module manipulator with variable stiffness for minimally invasive surgery," *Bioinspiration Biomimetics*, vol. 12, no. 5, Sep. 2017, Art. no. 056008.
[27] Y.-J. Kim, S. Cheng, S. Kim, and K. Iagnemma, "A novel layer jamming mechanism with tunable stiffness capability for minimally invasive surgery," *IEEE Trans. Robot.*, vol. 29, no. 4, pp. 1031–1042, Aug. 2013.
[28] J. Zhang et al., "Bioinspired continuum robots with programmable stiffness by harnessing phase change materials," *Adv. Mater. Technol.*, vol. 8, no. 6, Mar. 2023, Art. no. 2201616.
[29] J. Kim, W.-Y. Choi, S. Kang, C. Kim, and K.-J. Cho, "Continuously variable stiffness mechanism using nonuniform patterns on coaxial tubes for continuum microsurgical robot," *IEEE Trans. Robot.*, vol. 35, no. 6, pp. 1475–1487, Dec. 2019.
[30] R. J. Webster and B. A. Jones, "Design and kinematic modeling of constant curvature continuum robots: A review," *Int. J. Robot. Res.*, vol. 29, no. 13, pp. 1661–1683, 2010.
[31] B. A. Jones and I. D. Walker, "Kinematics for multisection continuum robots," *IEEE Trans. Robot.*, vol. 22, no. 1, pp. 43–55, Feb. 2006.
[32] A. Bajo and N. Simaan, "Kinematics-based detection and localization of contacts along multisegment continuum robots," *IEEE Trans. Robot.*, vol. 28, no. 2, pp. 291–302, Apr. 2012.
[33] M. M. Dalvand, S. Nahavandi, and R. D. Howe, "An analytical loading model for *n*-tendon continuum robots," *IEEE Trans. Robot.*, vol. 34, no. 5, pp. 1215–1225, Oct. 2018.
[34] R. E. Goldman, A. Bajo, and N. Simaan, "Compliant motion control for multisegment continuum robots with actuation force sensing," *IEEE Trans. Robot.*, vol. 30, no. 4, pp. 890–902, Aug. 2014, doi: 10.1109/TRO.2014.2309835.
[35] H. M. Le, P. T. Phan, C. Lin, L. Jiajun, and S. J. Phee, "A temperature-dependent, variable-stiffness endoscopic robotic manipulator with active heating and cooling," *Ann. Biomed. Eng.*, vol. 48, no. 6, pp. 1837–1849, Jun. 2020.
[36] J. Lussi et al., "A submillimeter continuous variable stiffness catheter for compliance control," *Adv. Sci.*, vol. 8, no. 18, Sep. 2021, Art. no. 2101290.
[37] X. Luo, D. Song, Z. Zhang, S. Wang, and C. Shi, "A novel distal hybrid pneumatic/cable-driven continuum joint with variable stiffness capacity for flexible gastrointestinal endoscopy," *Adv. Intell. Syst.*, vol. 5, no. 6, Jun. 2023, Art. no. 2200403.
[38] M. Brancadoro, M. Manti, F. Grani, S. Tognarelli, A. Menciassi, and M. Cianchetti, "Toward a variable stiffness surgical manipulator based on fiber jamming transition," *Frontiers Robot. AI*, vol. 6, p. 12, Mar. 2019.
[39] H. Wang and S. Zuo, "A novel variable-diameter-stiffness guiding sheath for endoscopic surgery," *IEEE Robot. Autom. Lett.*, vol. 8, no. 1, pp. 89–96, Jan. 2023.
[40] C. Li, X. Gu, X. Xiao, C. M. Lim, and H. Ren, "Flexible robot with variable stiffness in transoral surgery," *IEEE/ASME Trans. Mechatronics*, vol. 25, no. 1, pp. 1–10, Feb. 2020.
[41] P. Lloyd et al., "A magnetically-actuated coiling soft robot with variable stiffness," *IEEE Robot. Autom. Lett.*, vol. 8, no. 6, pp. 3262–3269, Jun. 2023.
[42] Z. Li, J. Li, Z. Wu, Y. Chen, M. Yeerbulati, and Q. Xu, "Design and hierarchical control of a homocentric variable stiffness magnetic catheter for multi-arm robotic ultrasound-assisted coronary intervention," *IEEE Trans. Robot.*, vol. 40, pp. 2306–2326, Mar. 2024.
[43] J. Chen et al., "A variable length, variable stiffness flexible instrument for transoral robotic surgery," *IEEE Robot. Autom. Lett.*, vol. 7, no. 2, pp. 3835–3842, Apr. 2022.

Jingyu Zhang (Member, IEEE) received the M.Eng. degree from Nanjing University of Science and Technology, Nanjing, Jiangsu, China. He is currently pursuing the Ph.D. degree in robotics with the Soft Medical Robotics Laboratory, Zhejiang University, Hangzhou, China. Previously, he has worked on medical ultrasound scanning systems. He is also developing novel different scale of soft continuum to augment the operation ability of surgeons.

Qin Fang is currently pursuing the Ph.D. degree with the School of Control Science and Engineering, Zhejiang University. During the master's degree, she studied with the School of Aeronautics and Astronautics, Zhejiang University. Her current research interests focus on the design, fabrication, and control of biomimetic soft robots.

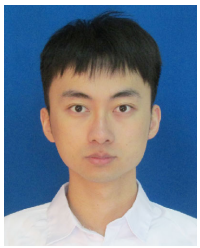

Lilu Liu received the B.Eng. degree from the School of Electrical Engineering and Automation, Harbin Institute of Technology, Harbin, China, in 2019. He is currently pursuing the Ph.D. degree with the College of Control Science and Engineering, Zhejiang University, Hangzhou, China. His research interests include medical image analysis, object pose estimation, and surgical robotics.

Rui Jin received the B.E. degree in mechanical design, manufacturing and automation from Northwestern Polytechnical University. He is currently pursuing the master's degree in control science and engineering with Zhejiang University under the supervision of Prof. Lu and Prof. Gao. His research interests include coaxial helicopter and autonomous flight.

Pingyu Xiang received the B.E. degree in mechatronic engineering from the School of Mechanical Engineering, Zhejiang University, where he is currently pursuing the M.E. degree in control science and engineering with the College of Control Science and Engineering. His research interests include continuum robotics, medical robotics, and machine learning.

Rong Xiong (Senior Member, IEEE) received the Ph.D. degree in control science and engineering from the Department of Control Science and Engineering, Zhejiang University, Hangzhou, China, in 2009. She is currently a Professor with the Department of Control Science and Engineering, Zhejiang University. Her latest research interests include motion planning and SLAM.

Yue Wang (Member, IEEE) received the Ph.D. degree in control science and engineering from the Department of Control Science and Engineering, Zhejiang University, Hangzhou, China, in 2016. He is currently an Associate Professor with the Department of Control Science and Engineering, Zhejiang University. His latest research interests include mobile robotics and robot perception.

Haojian Lu (Member, IEEE) received the B.Eng. degree in mechatronical engineering from Beijing Institute of Technology in 2015 and the Ph.D. degree in robotics from the City University of Hong Kong in 2019. He is currently a Professor with the State Key Laboratory of Industrial Control and Technology and Institute of Cyber-Systems and Control, Zhejiang University. His research interests include micro/nanorobotics, bioinspired robotics, medical robotics, micro aerial vehicle, and soft robotics.